Pristine Graphene Aerogels by Room-Temperature Freeze Gelation

*Yue Lin, Fei Liu, Gabriel Casano, Rupesh Bhavsar, Ian A. Kinloch, and Brian Derby**

A single sheet of graphene naturally possesses an extremely large specific surface area.[1] However, to enable the high surface area to be used in a practical device it must be packaged in a 3D volume. The highest surface area to volume ratio material based on chemically pure or pristine graphene (PG) is obtained using catalytic vapor deposition (CVD) to grow graphene on nanoporous templates, followed by template dissolution.[2] More cost effective nanoporous structures can be fabricated using graphene oxide (GO). These methods are more scalable but compromise on the properties because GO, after appropriate heat treatment, forms the defective reduced graphene oxide (rGO). Fabrication of 3D nanoporous structures using chemically exfoliated GO has been achieved by various methods[3] including aqueous freeze gelation[4–6] and hydrothermal processing.[7] Here we present a room temperature freeze gelation method to manufacture porous PG nanostructures from exfoliated material. The electrical properties of which are superior to conventional GO derived structures and approach those of CVD produced PG aerogels.

Room-temperature freeze gelation (RTFG) was originally developed by Halloran and co-workers for the manufacture of ceramics.[8] This processing route is similar to conventional aqueous freeze gelation (or freeze casting) but with the water replaced by an organic solvent selected to have a melting temperature greater than room temperature and a high vapor pressure. The material to be processed is mixed and dispersed in the solvent above its melting point, typically in the temperature range 50–120 °C and cooled to form a solid at room temperature. The solvent is selected to have a high vapor pressure above the solid at room temperature and thus rapidly sublimes at room temperature under ambient atmospheric conditions, leaving a porous solid of the original material.[8,9] The key advantages of this route over conventional aqueous freeze casting is that the broader range of solvents allow materials to be dispersed directly without surfactants or functionalization and, more significantly, the solid can be formed through conventional processing techniques prior to sublimation, whereas with aqueous routes one is restricted to purely freezing in a given shaped container.

A schematic of how the RTFG process is used for graphene aerogel manufacture is illustrated in **Figure 1**a. Briefly, PG flakes are dispersed to the required concentration in an appropriate solvent at elevated temperature, using sonication to form a stable dispersion. This dispersion is then used with an appropriate forming method, e.g., molding, extrusion or printing, and cooled to promote solidification. The resulting waxy solid contains a uniform suspension of PG flakes. The solvent sublimes at room temperature leaving a nanoporous graphene aerogel. RTFG has two principal advantages over conventional routes for the manufacture of graphene aerogels by aqueous freeze gelation: i) the solvent has a high vapor pressure and thus the sublimation process can be carried out under ambient conditions at room temperature and standard atmospheric pressure, ii) the wide range of potential solvents allows the selection of a fluid in which PG flakes can be readily dispersed. Two organic solvents have been used here to demonstrate the process: i) phenol (C_6H_6O: melting temperature, T_M = 40.5 °C, vapor pressure at room temperature, P_T = 47 Pa)[10] because of its prior use as a graphene exfoliant and solvent,[11] and ii) camphene ($C_{10}H_{16}$: T_M = 51.5 °C, P_T = 400 Pa)[8] because of its low toxicity (it is used in perfumes and medicines)[12] and its prior use for RTFG of ceramics.[8]

The microstructure of RTFG graphene aerogels obtained using both solvents is shown in Figure 1b,c. Solute rejection during solidification leads to solvent rich regions, which will create a characteristic microporosity of relatively large voids after sublimation, and graphene rich regions that solidify to a structure containing frustrated random packing of the PG flakes leading to an associated nanoporosity within the walls of the microporous structure. It is evident that the choice of solvent influences the microporous structure that is formed during initial solidification. The phenol derived aerogel has a characteristic lamellar structure that is similar to the aerogel microstructures formed during conventional aqueous freeze casting, for example, in Qiu's work.[5] In contrast the aerogel formed with camphene as a solvent shows an equiaxed microstructure with no directionality. This behavior is consistent with the solidification mechanism controlled by the anisotropy of the solid/liquid interfacial energy that leads to two classes of solidification microstructure.

i) If there is considerable variation in the interfacial energy there can be preferred directions of crystal growth that lead

Dr. Y. Lin, Dr. F. Liu, G. Casano, Dr. R. Bhavsar, Prof. I. A. Kinloch, Prof. B. Derby
School of Materials
University of Manchester
Oxford Rd, Manchester M13 9PL, UK
E-mail: brian.derby@manchester.ac.uk
R. Bhavsar
School of Chemistry
University of Manchester
Oxford Rd, Manchester M13 9PL, UK

DOI: 10.1002/adma.201602393

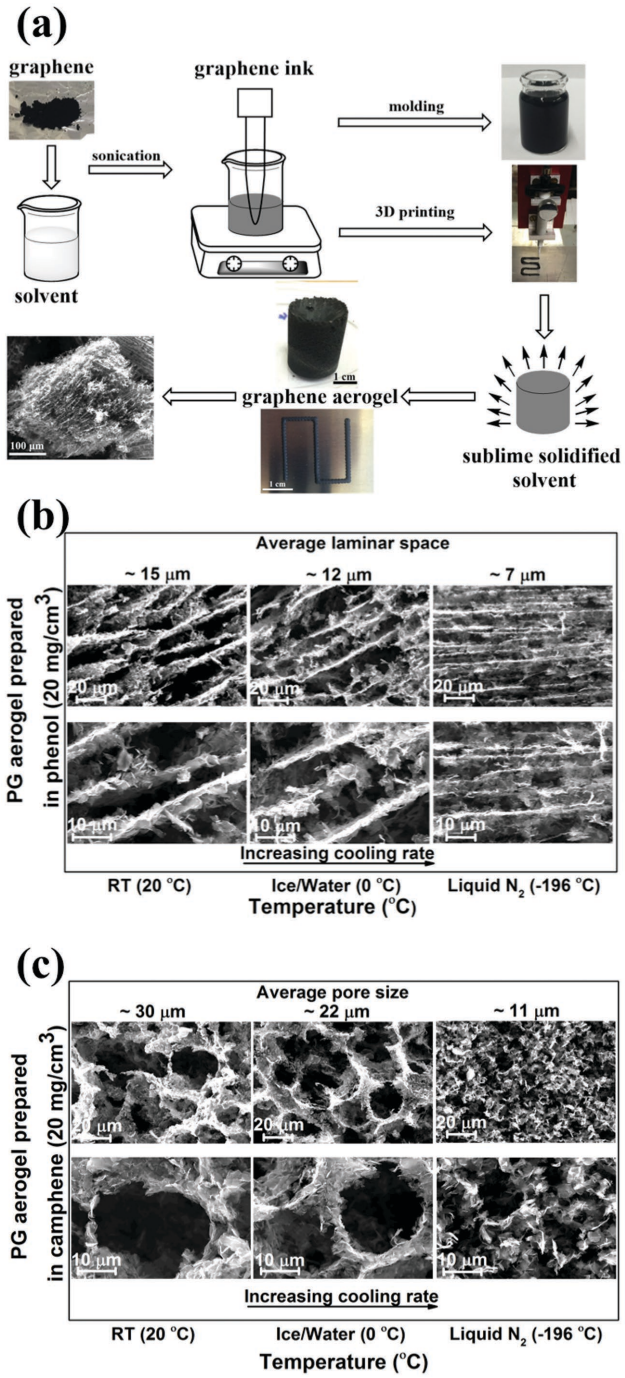

Figure 1. a) Schematic of the RTFG process. b,c) Scanning electron microscopy (SEM) images of phenol-based and camphene-based aerogel structures cooled using liquid N_2, an ice/water mixture, and at room temperature.

to well-developed crystal faces or facets during solidification, coupled with the influence of a temperature gradient this leads to the lamellar structure seen with phenol.

ii) If there is little variation in the interfacial energy solidification occurs with "rough interfaces" and the characteristic feature is the formation of a regular dendritic structure and an equiaxed structure between the dendrites, with directionality controlled principally by the temperature gradient as is the case during the solidification of metals. Camphene is well known as an organic material that solidifies with the same rough interfaces as found with metals[13] and this is reflected in the structures observed here.

With both mechanisms the microstructural length scale decreases as the solidification rate is increased.

Other methods used to fabricate GO aerogels have been adapted for use with additive manufacturing (3D printing) to enable complex shapes to be readily fabricated.[14–16] In these cases an aqueous suspension of GO was formed in a polymer solution to allow gelation of the structure after deposition. The subsequent gelled object has the water removed either by freeze drying or supercritical drying prior to an elevated temperature reduction to form a rGO aerogel. This three stage process was simplified by Zhang et al.[17] who printed an aqueous suspension of GO onto a chilled substrate to directly form a solid frozen object, reducing the process to two steps. Here, we have fabricated RTFG aerogel structures from pristine graphene by additive manufacturing at room temperature using PG-filled solvents (**Figure 2**a,b), confirming that RTFG can be used with processing methods in addition to moulding. Using the RTFG process enables the 3D printing process to be carried out at room temperature in a single step of printing and sublimation in the same apparatus. Figure 2c shows some cracking in the 3D printed structures, which have also been seen in other reports on 3D printed structures.[14,16]

The RTFG process can also be used with mixtures of graphene flakes and multiwalled carbon nanotubes (MWCNT), mixtures of rGO and MWCNT and with the addition of polymers in solution to increase the strength of the resulting aerogel (Figure 2e,f). The final aerogel microstructure is a function of the concentration of graphene, the solvents used, and the concentrations of polymer additives in suspension as well as the cooling rate as was shown in Figure 1. Further images of RTFG microstructures are presented in Figure S1–S7 of the Supporting Information illustrating the influence of: PG flake concentration, solvent, the addition of polymers in solution poly(vinyl alcohol) (PVA) and polyacrylonitrile (PAN), and the addition of multiwall or single wall carbon nanotubes (MWCNT and SWCNT).

Figure 3 shows the mechanical properties of the PG aerogels. We found that PG aerogels of graphene concentration 20 and 40 mg cm^{-3} had Young's modulus values of 7.7 ± 1.0 and 82.5 ± 4.0 kPa, respectively, and yield strength of 0.4 ± 0.01 and 2.1 ± 0.2 kPa (Figure 3c). However the addition of poly(vinyl alcohol) (PVA) in solution with the phenol prior to RTFG processing leads to a dramatic increase in aerogel Young's modulus to 553 ± 85 and 893 ± 82 kPa for 20 and 40 mg cm^{-3} PG aerogels, respectively, and yield strength of 25 ± 2 and 51 ± 3 kPa (Figure 3d). The PG aerogels have low values of stiffness and strength when compared with aerogels formed using GO and made by aqueous freeze casting or other related methods followed by elevated temperature reduction (Figure S8, Supporting Information). This is not surprising given that there is no mechanism for chemical bonding between the PG sheets in our aerogel. However, adding PVA in solution before RTFG processing leads to an order of magnitude increase of both the

Adv. Mater. 2016,
DOI: 10.1002/adma.201602393

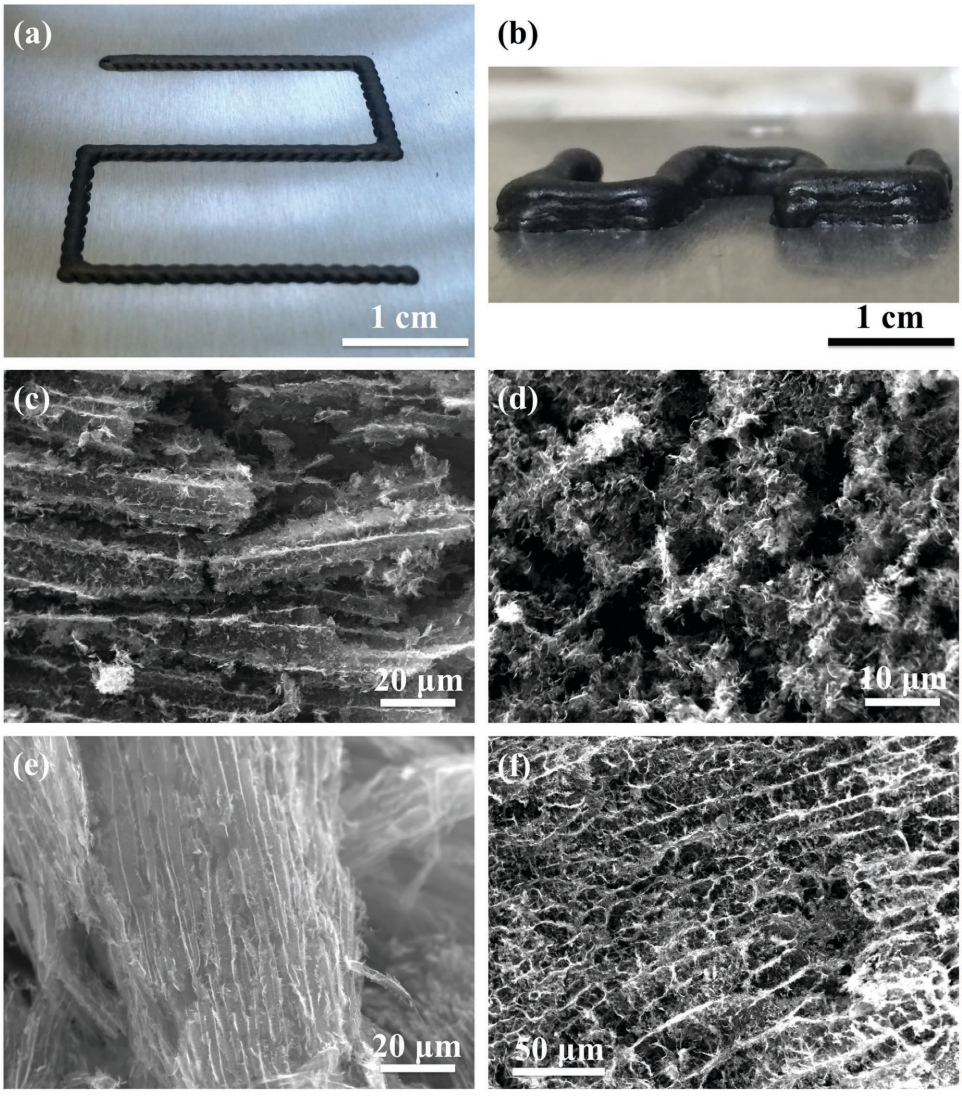

Figure 2. Printed graphene aerogel structures. a) A single layer robot cast track of PG aerogel using phenol as a solvent. b) Three layers of robot-cast PG aerogel demonstrating additive manufacture or 3D printing capability. c) SEM image of PG aerogel produced in phenol (40 mg cm^{-3}). d) PG prepared in camphene (40 mg cm^{-3}). e) PG/PVA (weight ratio: 4:1, 40 mg cm^{-3}). f) PG/MWCNT (weight ratio 4:1, 20 mg cm^{-3}).

aerogel Young's modulus and yield strength (Figure 3d) and these values are comparable with GO derived aerogels in the literature (Figure S8, Supporting Information).

Figure 4a shows Raman spectra from the PG flakes and the aerogel produced using phenol. The 2D peak shifts from 2666 cm^{-1} for PG to 2656 cm^{-1} for the aerogel. The 2D:G peak intensity ratio increases from 0.4 to 0.63. The shift and increase of the 2D peak suggests that the graphene in the aerogel is better quality than the PG, indicating that the PG may undergo further exfoliation during mixing. This is consistent with the presence of high quality few layer graphene sheets in the aerogel, without significant restacking and aggregation the PG flakes during processing. Raman spectroscopy was also used to verify that both of the solvents used during RTFG were fully removed through sublimation (Figure S9, Supporting Information).

Gas adsorption was used to determine the mean specific surface area of the aerogels (Figure 4b,c and Table S1, Supporting Information). The presence of a small quantity of MWCNT added to the PG suspension (20 wt.% MWCNT) significantly influences aerogel microstructure and physical properties. On sublimation the PG aerogel densifies to 6.5 mg cm^{-3} from its original solution density of 2.5 mg cm^{-3}. However the PG/MWCNT aerogel retains the density of the materials in liquid suspension, presumably because of the much greater compression stiffness of the MWCNT compared to the flexible PG flakes. The PG and PG/MWCNT aerogels have specific surface areas of approximately 400 and 700 m^2 g^{-1}, respectively (Figure 4c), which is also consistent with the presence of the MWCNT impeding densification. These surface area values are comparable with those from graphene aerogels fabricated by other methods.[14,18] The pore-size distribution lies in the 10–200 nm range shows a peak aerogel pore diameter of 73 nm for the PG aerogel and 83 nm for the PG/MWCNT aerogel (Figure 4c). Figure 4d shows the electrical conductivity of the

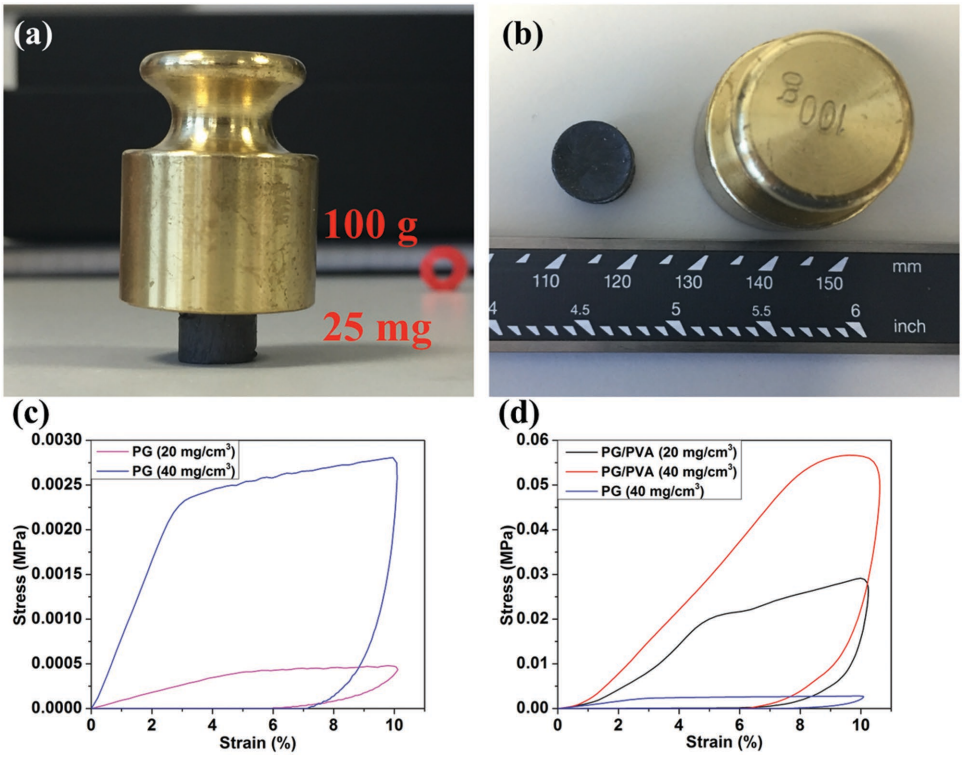

Figure 3. a,b) Images showing a 1 cm diameter PG/PVA aerogel disc (4:1 in weight, 40 mg cm^{-3} PG) supporting 100 g weight (4000 times of aerogel's weight) or a stress of approximately 13 kPa, stress–strain curves during load–unload cycle of a compression test. c) PG aerogel of concentration 20 mg cm^{-3} and 40 mg cm^{-3}. d) PG/PVA aerogel of concentration 20 and 40 mg cm^{-3} with 4:1 weight ratio of PG:PVA.

PG aerogel as a function of density with a maximum value of 9 S cm^{-1} at density of 20 mg cm^{-3}. Although the conductivity of the PG aerogel produced by RTFG is slightly inferior to those of similar density made by CVD onto sacrificial templates,[19] it is superior to those of rGO-based aerogels[20,21] and CNT foams[20] reported in the literature.

The electrical performance of these RTFG aerogels has been assessed for supercapacitor applications using a model two electrode configuration. **Figure 5** shows the electrical performance of supercapacitor structures, fabricated from four RTFG graphene electrodes made using the following starting compositions: PG, PG/MWCNT (4:1 ratio by weight), rGO and rGO/MWCNT (4:1 ratio by weight), using 1.0 M H_2SO_4 aqueous electrolyte. Note that the density of the PG and rGO aerogels are 6 mg cm^{-3} and that of the PG/MWCNT and rGO/MWCNT are 2.5 mg cm^{-3}, this is because the presence of the MWCNT prevents shrinkage of the aerogel during solvent sublimation. Figure 5a shows CV curves measured at a scan rate of 10 mV s^{-1}. The PG aerogel shows a flat response with no peaks as would be expected by a simple charge/discharge profile, however the CV response of the rGO, PG/MWCNT, and rGO/MWCNT all showed redox reactions due to the presence of oxygen containing groups in the rGO[22] and impurities in the MWCNT.[23] The overall shape of the CV curves is rectangular in profile, which indicates good double layer capacitance performance for all the aerogels fabricated. Further data showing CV curves at scan rates from 10 to 1000 mV s^{-1} are shown in Figure S10 of the Supporting Information. Galvanostatic cycling of the aerogels was performed at a current density of 1 A g^{-1} (Figure 5b). The aerogels exhibited nearly ideal triangular charge/discharge curve which indicates high charge mobility at the electrodes. Data obtained at current densities in the range 1–100 Ag^{-1} are presented in Figure S11 of the Supporting Information. Similar behavior was seen using the nonaqueous electrolyte 1.0 M tetraethyl ammonium tetrafluoroborate (TEABF)/propylene carbonate (Figure S12, Supporting Information). The specific capacitance (SC) of PG, rGO, PG/MWCNT, and rGO/MWCNT aerogels at a current density of 1 A g^{-1} is 123, 157, 167, and 305 F g^{-1} (Figure 5c). Furthermore, the energy density of PG, rGO, PG/MWCNT, and rGO/MWCNT at the current density of 1 A g^{-1} is 10.87, 13.45, 14.73, and 26.74 W h kg^{-1}, respectively (Figure 5d). Comparing our results with data from graphene aerogels reported in the literature (Table S3, Supporting Information), the aerogels prepared by RTFG show specific capacitance values comparable with the highest literature values.

The specific capacitance of PG/MWCNT and rGO/MWCNT aerogels are higher than that of the PG and rGO aerogels, which confirmed the role of MWCNT in the aerogels as both structural support and a separator which effectively prevents PG and rGO flakes from restacking and aggregating during solidification and sublimation, this is consistent with their influence on aerogel surface area (Figure 4b). We note that the specific capacitance of the PG-based aerogels is lower than that of the rGO-based aerogels at the current density of 1 A g^{-1}. This difference may be because PG is much easier to restack to a lower surface area material than rGO due to lack of functionality

Adv. Mater. **2016**,
DOI: 10.1002/adma.201602393

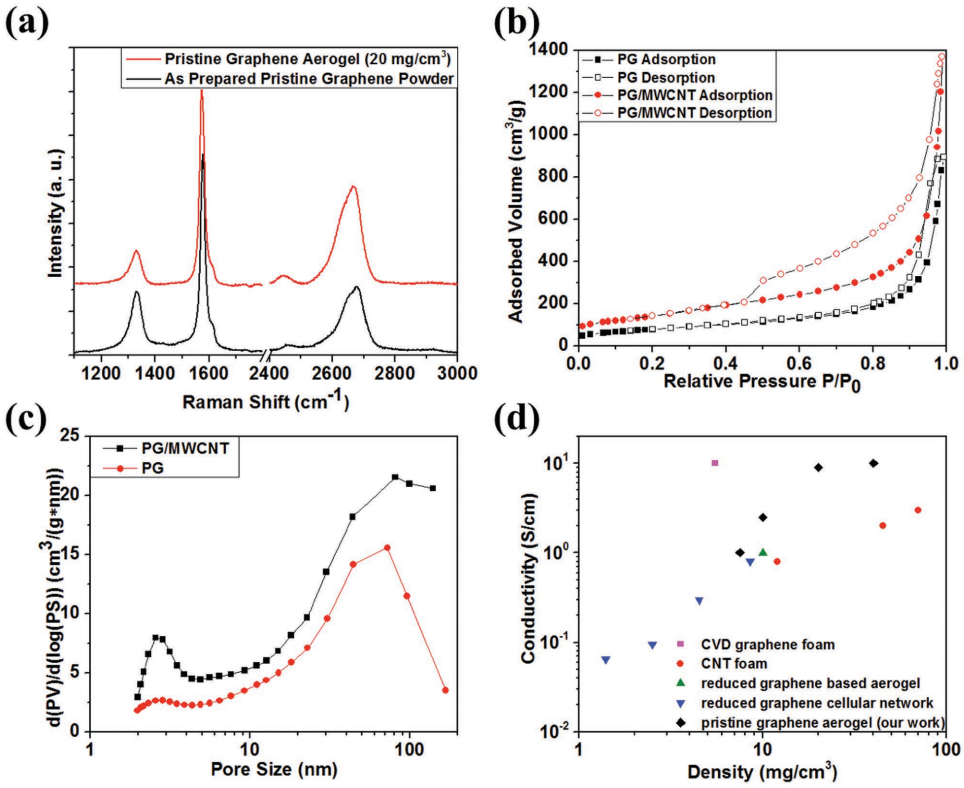

Figure 4. a) Raman spectra of as-prepared PG powder and PG aerogel (20 mg cm^{-3}). b) Nitrogen adsorption/desorption curve for PG aerogel (6 mg cm^{-3}) and PG/MWCNT (weight ratio 4:1, 2.5 mg cm^{-3}), c) Differential pore volume distribution of the PG and PG/MWCNT obtained by Barret–Joyner–Halenda (BJH) method. d) Electrical conductivity of PG aerogel versus density in comparison with the literature values of several low-density carbon nanomaterials (CVD-graphene aerogel,[19] CNT foam,[21] reduced-graphene-based aerogel,[20] and reduced-graphene cellular network[14]).

and more planar morphology, which leads to less exposed surface area. Furthermore, the residual functionality of rGO also enhances the apparent capacitance through introducing redox reactions. As is shown in Figure 5c, the specific capacitance of the aerogels decreases with increasing current density due to the internal resistance drop caused by current through the electrode. The PG aerogel has a lower internal resistance than rGO, thus internal losses will be reduced explaining the much smaller reduction in specific capacitance that occurs at higher discharge rates. It is remarkable that the PG/MWCNT aerogel gave a specific capacitance of 100 F g^{-1} at a fast scan rate of 100 A g^{-1}. PG showed much better performance under high current density. In comparison RGO/MWCNT gave only 72 F g^{-1} and RGO gave an even lower specific capacitance of 0.9 F g^{-1}. This significant improvement is believed to be due to the lower internal resistance of PG than that of rGO. The equivalent series resistance (ESR) of PG/MWCNT is 1.52 Ω, while the ESR of rGO/MWCNT is over three times higher which is 4.70 Ω. Thus, internal losses are reduced, explaining the much smaller reduction in specific capacitance that occurs at higher discharge rates. All the graphene aerogels exhibited excellent electrochemical stability and a high degree of reversibility (Figure 5e). The Coulombic efficiency of the initial capacitance for PG, rGO, PG/MWCNT, and rGO/MWCNT after 10000 cycles is 98.9%, 97.1%, 98.3%, and 97.7%, respectively.

Electrochemical impedance spectroscopy (EIS) of the aerogel-based supercapacitors was investigated and the results were plotted as Nyquist impedance curves (Figure 5f). The plots of the graphene-based aerogels consist of a small semicircle in the high frequency region and a rapidly rising line in the low frequency region, indicating a low electronic resistance and pristine capacitive behavior. The diameter of semicircle in high frequency is directly corresponding to the ESR of a supercapacitor.[24] The intercept at real part (Z') represents a combination of ionic resistance of electrolyte, intrinsic resistance of substrate, and contact resistance at the active material/current collector interface (R_s). The semicircle in the high-frequency range corresponds to the charge-transfer resistance (R_f) caused by the Faradaic reactions and the double-layer capacitance (C_{dl}) on the grain surface. C_f is the limit capacitance. The slope of the vertical line in low frequency region is the Warburg resistance (Z_w) which results from the frequency dependence of ion diffusion/transport in the electrolyte to the electrode surface.[25] From the Nyquist plots, the ESR of the PG, PG/MWCNT, rGO, and rGO/MWCNT aerogels are 1.83, 1.52, 5.29, and 4.70 Ω, respectively. Based on these values of ESR, the maximum power density of the PG, PG/MWCNT, rGO, and rGO/MWCNT was determined to be 21.86, 26.32, 8.51, and 7.56 kW kg^{-1}, respectively. The equivalent circuit and the values of the components required to fit to the Nyquist plots are given in Figure S13 and Table S3 of the Supporting Information.

To conclude, we have demonstrated that a RTFG process can be successfully used to fabricate aerogels from pristine graphene and reduced graphene oxide suspensions. The microstructure

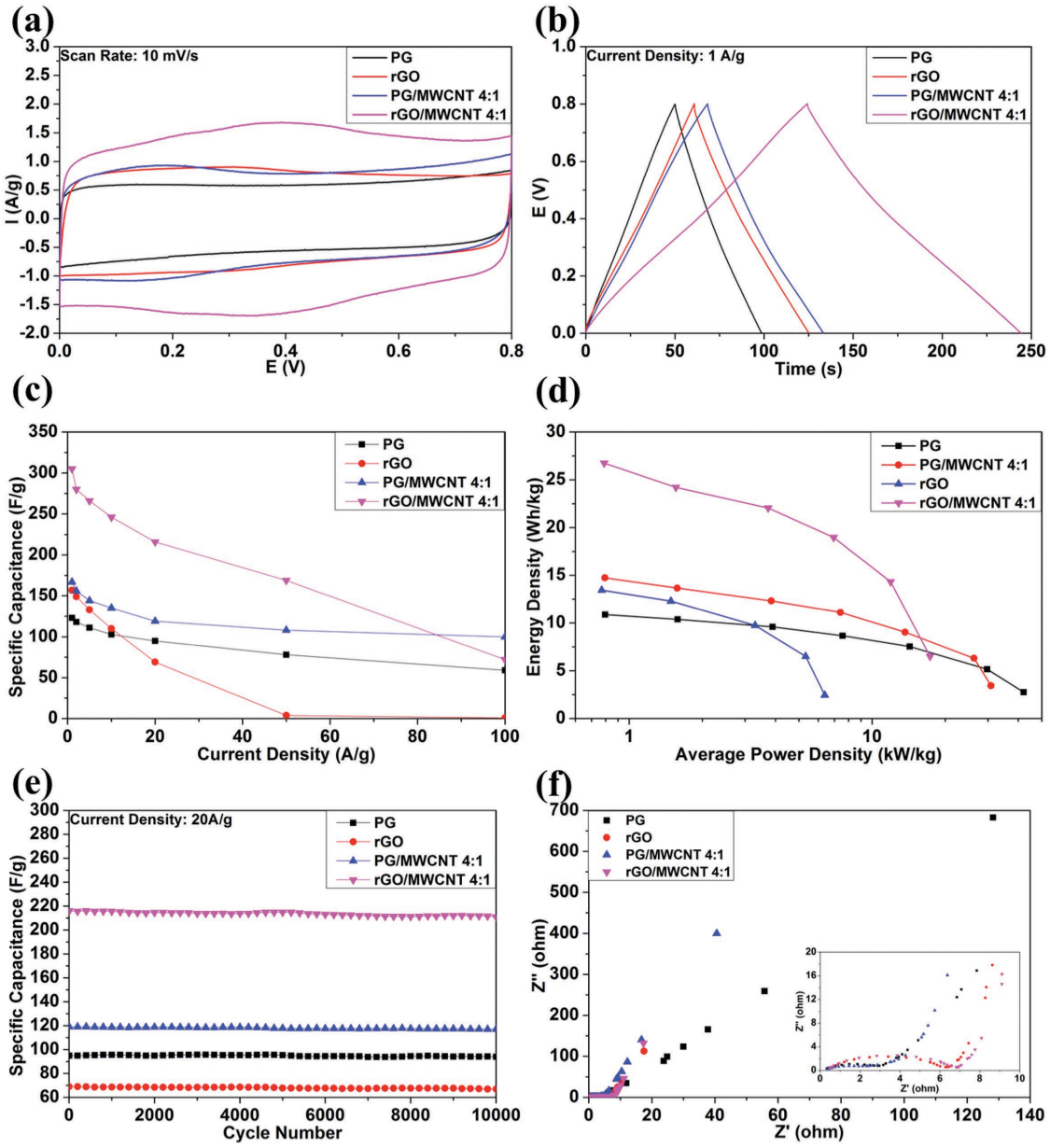

Figure 5. Electrochemical performance of graphene aerogels prepared by RTFG and tested in 1.0 M $H_2SO_{4\ (aqueous)}$. a) Cyclic voltammetry curves of the aerogels at the scan rate of 10 mV s^{-1}. b) Galvanostatic charge/discharge curves of the aerogels at the discharge current density of 1 A g^{-1}. c) Specific capacitance of the aerogels as a function of current densities. f) Ragone plot of the RTFG-aerogel-based supercapacitors. e) Cycling test of the aerogels at the current density of 20 A g^{-1} up to 10 000 cycles. f) Nyquist plots of the two-electrode supercapacitors based on the various aerogels.

of the resulting aerogel can be controlled by varying the solidification cooling rate through carrying out the process at temperatures below room temperature with an increase in cooling rate leading to a reduction in the microstructure length scale of the aerogel. We have demonstrated that the process is possible using phenol and camphene as suitable solvents but we believe that there is a wide range of solvents with appropriate graphene solubility and vapor pressure that could also be used. The strength and stiffness of the resulting aerogels are significantly smaller than those produced using GO as the starting material where the high-temperature reduction stage to form rGO generates stronger interflake chemical bonds, however the decrease in strength is compensated by an improved electrical performance. The process is compatible with a number of shaping methods including moulding, 3D printing and inkjet printing. We believe that it will also be compatible with a larger range of processing methods used with ceramic-filled waxes including tape casting, extrusion, and calendaring. By allowing the use of pristine graphene and reduced graphene oxide in the starting suspension, we are able to produce aerogels with conductivities comparable to those previously only attainable via CVD onto a nanoporous template. We have

Adv. Mater. **2016**,
DOI: 10.1002/adma.201602393

demonstrated that these aerogels can be used as electrodes in model supercapacitors and have shown that the performance of the material is comparable with the best results in terms of specific capacitance and power/energy density achievable from other graphene-based materials.

Experimental Section

Aerogel Preparation: PG sheets were prepared from graphite nanoplatelets (XG Sciences Ltd., xGnP M-5) using a liquid-phase exfoliation method developed by Lin et al.[11] GO aqueous dispersions and rGO were prepared from natural graphite (Graphexel, 2369) following methods described elsewhere.[26] The aerogels were prepared in various concentrations (2–100 mg cm^{-3}) by using a range of carbon sources (pristine graphene, reduced graphene oxide, multiwalled carbon nanotubes, single-walled carbon nanotubes or mixtures of two or more of the above), using two solvent bases, phenol and camphene (Sigma–Aldrich, Dorset, UK). Typically, 100 mg of graphene and 5 mL solvent were mixed at 50 °C (phenol) or 60 °C (camphene) for 30 min. Afterward, the mixture was sonicated (Q700 Probe, QSonica, Newtown, CT, USA) with a power of 5 W for 15 min in a 50 °C oil bath. The mixture was then solidified in a glass mold at either ambient room temperature (20 °C), in an ice/water bath (0 °C), or cooled in liquid nitrogen (–196 °C). The solidified object was removed from the mold at room temperature. The aerogel was obtained by full sublimation of the solidified solvent in a fume hood at room temperature.

3D Printing: The sonicated mixture was used as an ink without modification and directly transferred to a 3 mL Luer Lok syringe with a smooth flow tapered nozzle (159 µm inner diameter) attached. The ink was heated to 60 °C to ensure it retained the liquid state during processing. The 3D objects were printed using a robotic deposition device (I&J7300-LF Robotics, Fisnar Inc., Pine Brook, NJ, USA). The 3D printed structures were solidified on the substrate held at room temperature and subsequently sublimed in a fume hood at room temperature.

Characterization: The microstructures of the graphene-based aerogels were investigated using scanning electron microscopy (XL30 FEGSEM, FEI, Eindhoven, The Netherlands). The electrical conductivity of the aerogels was measured using a standard 4-point probe method by a NumetriQ PSM1735 analyzer (Newtons4th Ltd., Loughborough, UK). The densities of the aerogels were determined by measuring their dimensions using a digital vernier caliper and their mass using a balance with 0.001 mg accuracy. The nitrogen adsorption isotherm measurements were performed at –196 °C using an ASAP 2020 (Micromeritics, Norcross, GA, USA) surface area and porosity analyzer. The Raman spectra were taken using a Renishaw 2000 Raman spectrometer system (Renishaw, Wooton-under-Edge, UK) with a HeNe laser (1.96 eV, 633 nm). The mechanical performance of PG-based aerogels was measured using dynamic mechanical analyzer (DMA Q800, TA Instruments, New Castle, DA, USA) under compression mode at a loading and unloading speed of 1 mm min^{-1}.

For supercapacitor tests, the aerogel (2 mg) was directly attached to 325 mesh stainless-steel gauze as working electrodes. The test was carried out in a two-electrode system. The working electrodes separated by a filter paper was firmly pressed by two poly(methyl methacrylate) (PMMA) slides to assemble a cell. The cell was then dipped in 1.0 M H_2SO_4 electrolyte (Sigma–Aldrich) to perform cyclic voltammetry and galvanostatic charge–discharge over the potential range of 0 to 0.8 V. Another cell was also dipped in 1.0 M tetraethyl ammonium tetrafluoroborate (TEABF)/propylene carbonate (Sigma–Aldrich) organic electrolyte to perform cyclic voltammetry and galvanostatic charge–discharge over the potential range of 0–2 V. Electrochemical impedance spectroscopy was performed by an AC voltage of 0.2 V with 5 mV amplitude over a frequency range between 10 mHz and 10 kHz. All tests were carried out using an Ivium electrochemical workstation (Ivium Technologies, Eindhoven. Netherlands).

Supporting Information

Supporting Information is available from the Wiley Online Library or from the author.

Acknowledgements

This research was funded through the following sources: EPSRC grantsEP/I023879/1 and EP/K016954/1; the EU Graphene Flagship (Grant Agreement No. 604391). G.C. would like to acknowledge an EPSRC Doctoral Training Studentship awarded through the GrapheneNOWNANO CDT.

Received: May 5, 2016
Revised: June 10, 2016
Published online:

[1] a) A. K. Geim, K. S. Novoselov, *Nat. Mater.* **2007**, *6*, 183; b) M. D. Stoller, S. J. Park, Y. W. Zhu, J. H. An, R. S. Ruoff, *Nano Lett.* **2008**, *8*, 3498.
[2] M. Mecklenburg, A. Schuchardt, Y. K. Mishra, S. Kaps, R. Adelung, A. Lotnyk, L. Kienle, K. Schulte, *Adv. Mater.* **2012**, *24*, 3486.
[3] S. Nardecchia, D. Carriazo, M. L. Ferrer, M. C. Gutierrez, F. del Monte, *Chem. Soc. Rev.* **2013**, *42*, 794.
[4] X. T. Zhang, Z. Y. Sui, B. Xu, S. F. Yue, Y. J. Luo, W. C. Zhan, B. Liu, *J. Mater. Chem.* **2011**, *21*, 6494.
[5] L. Qiu, J. Z. Liu, S. L. Y. Chang, Y. Z. Wu, D. Li, *Nat. Commun.* **2012**, *3*, 1241.
[6] Q. Zheng, Z. Cai, Z. Ma, C. Gong, *ACS Appl. Mater. Interfaces* **2015**, *7*, 3263.
[7] a) Z. S. Wu, Y. Sun, Y. Z. Tan, S. B. Yang, X. L. Feng, K. Mullen, *J. Am. Chem. Soc.* **2012**, *134*, 19532; b) Y. Q. Qian, I. M. Ismail, A. Stein, *Carbon* **2014**, *68*, 221; c) L. Zhang, F. Zhang, X. Yang, G. K. Long, Y. P. Wu, T. F. Zhang, K. Leng, Y. Huang, Y. F. Ma, A. Yu, Y. S. Chen, *Sci. Rep.* **2013**, *3*, 408.
[8] a) K. Araki, J. W. Halloran, *J. Am. Ceram. Soc.* **2004**, *87*, 1859; b) K. Araki, J. W. Halloran, *J. Am. Ceram. Soc.* **2005**, *88*, 1108.
[9] K. Araki, J. W. Halloran, *J. Am. Ceram. Soc.* **2004**, *87*, 2014.
[10] a) T. E. Daubert, R. P. Danner, *Physical and Thermodynamic Properties of Pure Chemicals Data Collection*, Taylor and Francis, New York, USA **1989**; b) A. H. Jones, *J. Chem. Eng. Data* **1960**, *5*, 196.
[11] Y. Lin, J. Jin, O. Kusmartsevab, M. Song, *J. Phys. Chem. C* **2013**, *117*, 17237.
[12] R. Höfer, in *Industrial Biorefineries & White Biotechnology*, (Eds: A. Pandey, R. Höfer, M. Taherzadeh, M. Nampoothiri, C. Larroche), Elsevier, Oxford, UK **2015**, p. 127.
[13] K. A. Jackson, J. D. Hunt, *Acta Metall.* **1965**, *13*, 1212.
[14] S. Barg, F. M. Perez, N. Ni, P. de V. Pereira, R. C. Maher, E. Garcia-Tunon, S. Eslava, S. Agnoli, C. Mattevi, E. Saiz, *Nat. Commun.* **2014**, *5*, 4328
[15] E. Garcia-Tunon, S. Barg, J. Framco, R. Bell, S. Eslava, E. D'Elia, R. C. Maher, F. Guitian, E. Saiz, *Adv. Mater.* **2015**, *27*, 1688.
[16] C. Zhu, T. Y-J. Han, E. B. Duoss, A. M. Golobic, J. D. Kuntz, C. M. Spadaccini, M. A. Worsley, *Nat. Commun.* **2015**, *6*, 6962.
[17] Q. Zhang, F. Zhang, S. P. Medarametla, H. Li, C. Zhou, D. Lin, *Small* **2016**, *12*, 1702.
[18] a) Z.-Y. Sui, Y.-N. Meng, P.-W. Xiao, Z.-Q. Zhao, Z.-X. Wei, B.-H. Han, *ACS Appl. Mater. Interfaces* **2015**, *7*, 1431; b) S. M. Jung, D. L. Mafra, C.-T. Lin, H. Y. Jung, J. Kong, *Nanoscale* **2015**, *7*, 4386.
[19] Z. P. Chen, W. C. Ren, L. B. Gao, B. L. Liu, S. F. Pei, H. M. Cheng, *Nat. Mater.* **2011**, *10*, 424.

[20] M. A. Worsley, P. J. Pauzauskie, T. Y. Olson, J. Biener, J. H. Satcher, T. F. Baumann, *J. Am. Chem. Soc.* **2010**, *132*, 14067.
[21] M. A. Worsley, S. O. Kucheyev, J. H. Satcher, A. V. Hamza, T. F. Baumann, *Appl. Phys. Lett.* **2009**, *94*, 073115.
[22] a) F. Liu, S. Y. Song, D. F. Xue, H. J. Zhang, *Adv. Mater.* **2012**, *24*, 1089; b) F. Beguin, K. Szostak, G. Lota, E. Frackowiak, *Adv. Mater.* **2005**, *17*, 2380.
[23] M. Pumera, A. Ambrosi, E. L. K. Chng, *Chem. Sci.* **2012**, *3*, 3347.
[24] B. N. M. Dolah, M. A. R. Othman, M. Deraman, N. H. Basri, R. Farma, I. A. Talib, M. M. Ishak, *J. Phys. Conf. Ser.* **2013**, *431*, 012015
[25] Z. Fan, J. Yan, T. Wei, L. Zhi, G. Ning, T. Li, F. Wei, *Adv. Funct. Mater.* **2011**, *21*, 2366.
[26] a) Y. X. Xu, H. Bai, G. W. Lu, C. Li, G. Q. Shi, *J. Am. Chem. Soc.* **2008**, *130*, 5856; b) Y. Zhou, Q. L. Bao, L. A. L. Tang, Y. L. Zhong, K. P. Loh, *Chem. Mater.* **2009**, *21*, 2950.

Adv. Mater. **2016**,
DOI: 10.1002/adma.201602393